

---

This is an electronic reprint of the original article.  
This reprint may differ from the original in pagination and typographic detail.

Philip, Anish; Jussila, Topias; Obenluneschloß, Jorit; Zanders, David; Preischel, Florian; Kinnunen, Jussi; Devi, Anjana; Karppinen, Maarit

## Conformal Zn-Benzene Dithiol Thin Films for Temperature-Sensitive Electronics Grown via Industry-Feasible Atomic/Molecular Layer Deposition Technique

*Published in:*  
Small

*DOI:*  
[10.1002/smll.202402608](https://doi.org/10.1002/smll.202402608)

Published: 03/10/2024

*Document Version*  
Publisher's PDF, also known as Version of record

*Published under the following license:*  
CC BY-NC

*Please cite the original version:*  
Philip, A., Jussila, T., Obenluneschloß, J., Zanders, D., Preischel, F., Kinnunen, J., Devi, A., & Karppinen, M. (2024). Conformal Zn-Benzene Dithiol Thin Films for Temperature-Sensitive Electronics Grown via Industry-Feasible Atomic/Molecular Layer Deposition Technique. *Small*, 20(40), Article 2402608. <https://doi.org/10.1002/smll.202402608>

---

This material is protected by copyright and other intellectual property rights, and duplication or sale of all or part of any of the repository collections is not permitted, except that material may be duplicated by you for your research use or educational purposes in electronic or print form. You must obtain permission for any other use. Electronic or print copies may not be offered, whether for sale or otherwise to anyone who is not an authorised user.

# Conformal Zn-Benzene Dithiol Thin Films for Temperature-Sensitive Electronics Grown via Industry-Feasible Atomic/Molecular Layer Deposition Technique

Anish Philip, Topias Jussila, Jorit Obenluneschloß, David Zanders, Florian Preischel, Jussi Kinnunen, Anjana Devi, and Maarit Karppinen\*

The atomic/molecular layer deposition (ALD/MLD) technique combining both inorganic and organic precursors is strongly emerging as a unique tool to design exciting new functional metal-organic thin-film materials. Here, this method is demonstrated to work even at low deposition temperatures and can produce highly stable and conformal thin films, fulfilling the indispensable prerequisites of today's 3D microelectronics and other potential industrial applications. This new ALD/MLD process is developed for Zn-organic thin films grown from non-pyrophoric bis-3-(*N,N*-dimethylamino)propyl zinc [Zn(DMP)<sub>2</sub>] and 1,4-benzene dithiol (BDT) precursors. This process yields air-stable Zn-BDT films with appreciably high growth per cycle (GPC) of 4.5 Å at 60 °C. The Zn/S ratio is determined at 0.5 with Rutherford backscattering spectrometry (RBS), in line with the anticipated (Zn–S–C<sub>6</sub>H<sub>6</sub>–S)<sub>n</sub> bonding scheme. The high degree of conformality is shown using lateral high-aspect-ratio (LHAR) test substrates; scanning electron microscopy (SEM) analysis shows that the film penetration depth (PD) into the LHAR structure with cavity height of 500 nm is over 200 µm (i.e., aspect-ratio of 400). It is anticipated that the electrically insulating metal-organic Zn-BDT thin films grown via the solvent-free ALD/MLD technique, can be excellent barrier layers for temperature-sensitive and flexible electronic devices.

emerging toward future application areas ranging from micro- and optoelectronics to energy conversion and storage.<sup>[1]</sup> Robust ALD/MLD processes have been developed for a wide variety of inorganic and organic precursor combinations, motivated by the intriguing possibility to combine the best parts of these two worlds to create new combinatorial functional properties.<sup>[1–4]</sup> Like in case of the parent ALD (atomic layer deposition) technique,<sup>[5,6]</sup> the combined ALD/MLD method has been shown to enable precise control over the film thickness, composition, and structure, owing to its unique sequential precursor pulsing scheme and the self-limiting nature of the precursor surface adsorption. Excitingly, through the gas-surface reactions of the sequentially pulsed inorganic and organic precursors, entirely novel hybrid materials that are otherwise difficult to achieve may be realized.<sup>[7,8]</sup>

One of the anticipated application areas for the ALD/MLD-grown metal-organic thin films is in the barrier coatings to protect various devices against environmental

damage caused, for example, by moisture, oxygen, or corrosive gases; for example, in microelectronics sensitive device parts are often encapsulated with such a protective barrier coating.<sup>[9–11]</sup> For the barrier-coating application, the films should

## 1. Introduction

Currently, the atomic/molecular layer deposition (ALD/MLD) technique yielding hybrid inorganic-organic thin films is strongly

A. Philip, T. Jussila, M. Karppinen  
Department of Chemistry and Materials Science  
Aalto University  
Espoo FI-00076, Finland  
E-mail: [maarit.karppinen@aalto.fi](mailto:maarit.karppinen@aalto.fi)

 The ORCID identification number(s) for the author(s) of this article can be found under <https://doi.org/10.1002/sml.202402608>

© 2024 The Author(s). Small published by Wiley-VCH GmbH. This is an open access article under the terms of the [Creative Commons Attribution-NonCommercial](#) License, which permits use, distribution and reproduction in any medium, provided the original work is properly cited and is not used for commercial purposes.

DOI: 10.1002/sml.202402608

A. Philip, J. Kinnunen  
Chipmetrics Ltd  
Joensuu 80130, Finland  
J. Obenluneschloß, D. Zanders, F. Preischel, A. Devi  
Inorganic Materials Chemistry  
Ruhr University Bochum  
44801 Bochum, Germany

A. Devi  
Leibniz Institute for Solid State and Materials Research  
01069 Dresden, Germany

A. Devi  
Chair of Materials Chemistry  
Dresden University of Technology  
01069 Dresden, Germany

be pinhole-free, homogeneous, and conformal on very complex 3D architectures.<sup>[12–14]</sup> In the case of flexible devices, an additional issue concerns the mechanical properties of the barrier coating; here the benefits of the ALD/MLD inorganic-organic coatings over the conventional ALD inorganic films are evident as the organic components can significantly improve mechanical flexibility.<sup>[13,15–17]</sup> Finally, efficient low-temperature ALD/MLD processes are needed to comply with the requirements of temperature-sensitive devices.

Up to date, so-called metalcone (alucones, zincones, etc.)<sup>[18–24]</sup> ALD/MLD thin films that are metal alkoxides grown from aliphatic or aromatic diols, have been most widely explored for the flexible barrier layer applications.<sup>[11,20,25–27]</sup> However, a typical drawback of these alkoxide thin films is their tendency to degrade in ambient conditions.<sup>[22,28–31]</sup> Furthermore, reports on the conformality of these metal-organic thin films are sparse.<sup>[32,33]</sup> Indeed, the 3D geometries and high-aspect ratio features in today's microelectronics pose increasingly strict requirements not only for the conformality (uniform film thickness and composition) but also for the film penetration depth (how deep the film can grow in high aspect ratio cavities).<sup>[34–36]</sup>

In the present contribution, we report a new low-temperature ALD/MLD process developed for Zn-benzene dithiol (Zn-BDT) thin films to address the aforementioned challenges; a schematic presentation of the deposition process and the reactor used can be found in Figure S1 (Supporting Information). First, the low deposition temperature is made possible by selecting readily evaporable and reactive precursors, in particular the non-pyrophoric bis-3-(*N,N*-dimethylamino)propyl zinc(II) [Zn(DMP)<sub>2</sub>]<sup>[14]</sup> instead of the commonly employed pyrophoric diethyl zinc (DEZ),<sup>[30,37,38]</sup> and sulfur-based benzene-1,4-dithiol (BDT) instead of the commonly employed alcohols and carboxylic acids.<sup>[18,21,31,37–42]</sup> Besides its relatively high volatility (Figure S2, Supporting Information)<sup>[43]</sup> required for the low-temperature MLD, another favorable aspect of BDT is the thiol group that was anticipated to enhance the stability of the resultant Zn-organic thin film.<sup>[44]</sup> The [Zn(DMP)<sub>2</sub>] precursor has been previously used in ALD/MLD in combination with hydroquinone,<sup>[31]</sup> while the organic dithiol BDT has been previously challenged in ALD/MLD in combination with [Cu(dmap)<sub>2</sub>].<sup>[43]</sup> Of these previously reported processes, the former suffered from limited film stability due to the aromatic diol precursor, and the latter process was limited to deposition temperatures >80 °C due to the sublimation temperature (60 °C) of Cu(dmap)<sub>2</sub>. Here – besides the appreciably low deposition temperature – we will demonstrate using lateral high-aspect-ratio (LHAR)<sup>[33]</sup> test structures that the Zn-BDT films grow in a highly conformal manner and are distinctly stable upon long-term storage in ambient conditions.

## 2. Results and Discussion

The [Zn(DMP)<sub>2</sub>] + BDT deposition process was investigated by systematically changing the deposition parameters (deposition temperature and precursor pulse and purge lengths) as shown in Figure 1. First, the process was investigated within the temperature range from 50 to 100 °C, the lowest feasible deposition temperature defined by the precursor sublimation temperatures (35 °C for both precursors). The resultant thin films appeared homogeneous from visual inspection, and were found to be amor-

phous from both GI-XRD (grazing incidence X-ray diffraction) and SEM (scanning electron microscopy) measurements, as no macroscopic grains were seen in the latter (Figure S3, Supporting Information). From Figure 1a, the GPC (growth-per-cycle) value decreases with increasing deposition temperature from 5.1 Å at 50 °C to 3.1 Å at 100 °C. Several reasons for this trend – common to most of the ALD/MLD processes – have been suggested in literature: i) condensation or irreversible physisorption of the organic or the metal precursor molecules which may result in additional reaction sites at low temperatures, ii) increased desorption of the precursor molecules at higher temperatures, and iii) decomposition of the precursor molecules to volatile products at elevated temperatures.<sup>[21,45,46]</sup> Of these three possible phenomena, the potential precursor decomposition issue could be ruled out, as the thermal stability was found sufficient for both the metal<sup>[14]</sup> and the organic precursor from thermogravimetric/differential thermal analysis (Figure S2, Supporting Information) in the deposition temperature range investigated. The condensation/physorption of the precursor molecules can be excluded as well since clear saturation was obtained for both precursors (Figure 1b); increasing the pulse length did not affect the GPC. Most probably the decreasing GPC with increased deposition temperature is caused by an increased desorption rate of precursor molecules which limits the likelihood for surface reactions to occur via irreversible chemisorption and hence limits film growth.<sup>[47]</sup> Nevertheless, a rather stable GPC trend was established for a deposition temperature range of 60–70 °C. Consequently, for the subsequent experiments, we fixed the deposition temperature to 60 °C.

The data collected in Figure 1b for the GPC values obtained with various precursor pulse lengths indicate that with the precursor pulse/purge sequence, 3 s [Zn(DMP)<sub>2</sub>]/20 s N<sub>2</sub>/3 s BDT/20 s N<sub>2</sub>, chosen for the rest of the experiments, the surface saturation condition is achieved. Noteworthy, only very small variations in GPC are seen within the entire precursor pulse length ranges investigated. Moreover, the GPC value remained unchanged upon increasing the N<sub>2</sub> purge length for both precursors (Figure 1c). Finally, from Figure 1d the linear dependency ( $R^2 = 0.998$ ) of film thickness on the number of ALD/MLD cycles applied can be verified for our [Zn(DMP)<sub>2</sub>] + BDT process; the GPC value calculated from the slope of the fitted line is 4.5 Å, which is less than the length of a (Zn–S–C<sub>6</sub>H<sub>4</sub>–S)<sub>n</sub> layer predicted with Chem3D software ( $\approx 7.5$  Å). This is characteristic for ALD and ALD/MLD processes since only partial surface coverage is typically attained during one deposition cycle.

Interestingly, this GPC value is significantly higher than the value (3.2 Å) obtained for the corresponding hydroquinone (HQ; benzene-1,4-diol) based [Zn(DMP)<sub>2</sub>] + HQ process at the same deposition temperature in our earlier work.<sup>[31]</sup> The optimal (Zn–S–C<sub>6</sub>H<sub>4</sub>–S) “structure unit” is roughly 1 Å longer than the optimal (Zn–O–C<sub>6</sub>H<sub>4</sub>–O) unit. However, it is unlikely that this size difference would solely explain the different GPC values as it would essentially require all the organic molecules to be aligned vertically with respect to the substrate. A significant contribution to the GPC is expected from the difference in reactivities of the organic precursors. Better reactivity of the S–H groups in BDT toward the [Zn(DMP)<sub>2</sub>] precursor in comparison to the O–H groups in HQ results from the more nucleophilic/acidic nature of the thiol group.

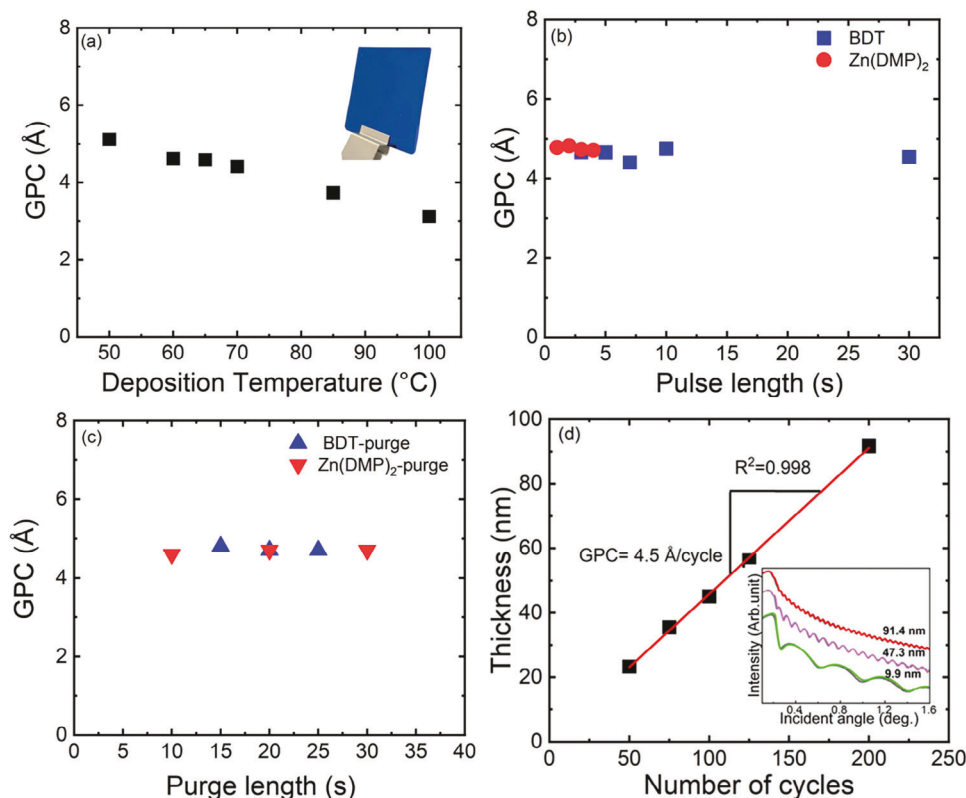


**Figure 1.** ALD/MLD characteristics of the  $[\text{Zn}(\text{DMP})_2] + \text{BDT}$  process: a) GPC versus deposition temperature, b) saturation of GPC value with individually increased precursor pulse lengths, c) GPC versus purge lengths after precursor pulses, d) linear dependence of film thickness on the number of ALD/MLD cycles applied. The inserts in (a) and (d) display, respectively, a photograph of a 100-nm Zn-BDT film grown on  $3 \times 3 \text{ cm}^2$  silicon wafer indicating the visual homogeneity of the film, and representative XRR curves obtained for Zn-BDT films with different thicknesses. The black lines in XRR are fitted patterns. In (b), (c), and (d), the deposition temperature was  $60 \text{ }^\circ\text{C}$ , and for (a) and (d) the pulse/purge sequence was: 3 s  $[\text{Zn}(\text{DMP})_2]/20 \text{ s N}_2/3 \text{ s BDT}/20 \text{ s N}_2$ .

The film density was estimated from the XRR (X-ray reflectivity) data for three Zn-BDT thin films with different thicknesses (Figure 1d, insert): a constant density value of  $\approx 1.69 \text{ g cm}^{-3}$  was obtained irrespective of the film thickness. This value is in the range typical for other ALD/MLD-grown metal-organic thin films.<sup>[2,48–50]</sup> We also investigated the possible influence of the  $[\text{Zn}(\text{DMP})_2]$  precursor pulse length on the density, but no significant effect was found. For the film roughness investigation, AFM (atomic force microscopy) imaging was utilized (Figure S4, Supporting Information). Appreciably low RMS (root-mean-square) roughness values were obtained, that is, 0.8 and 0.5 nm for 10 and 100-nm thick films, respectively. This is important considering the potential application of these thin films as barrier coatings.<sup>[51]</sup>

The targeted metal-organic bonding scheme was verified with both FTIR (Fourier transform infrared) and Raman spectroscopy for a representative Zn-BDT thin film (Figure 2). From the FTIR spectrum, the aimed reaction between the  $[\text{Zn}(\text{DMP})_2]$  and BDT precursors can be concluded from the complete disappearance of the characteristic  $\nu(\text{S}-\text{H})$  stretching vibration peak seen at  $2557 \text{ cm}^{-1}$  for the BDT precursor, and the appearance of the  $\nu(\text{Zn}-\text{S})$  stretching peak at  $636 \text{ cm}^{-1}$  for the Zn-BDT thin film. The aromatic  $\nu(\text{C}=\text{C})$  stretching vibration at  $1472 \text{ cm}^{-1}$  and the  $\gamma(\text{C}-\text{H})$  bending vibration at  $806 \text{ cm}^{-1}$  confirm the presence of aromatic rings in the Zn-BDT film.<sup>[43,52]</sup> Similarly, the Raman

spectrum shows all the Stokes lines expected for the aromatic ring. However, the  $\nu(\text{S}-\text{H})$  stretching vibration at  $2527 \text{ cm}^{-1}$  indicates the presence of some unreacted BDT precursor in our Zn-BDT films (Figure 2b, insert);<sup>[53]</sup> the extremely low peak intensity suggests that the portion of the precursor left unreacted is relatively small.<sup>[43]</sup>

Elemental composition was investigated for the Zn-BDT films using RBS (Rutherford backscattering spectrometry) technique (Figure 3). For the study, two thin-film samples with different thicknesses (10 and 100 nm) were selected, and the results revealed the Zn/S ratio of 0.5, as expected for a structure where each zinc atom is bound to two sulfur atoms. Moreover, the carbon content (67%) also matched well with the expected value, indicating that the  $[\text{Zn}(\text{DMP})_2] + \text{BDT}$  process indeed yields high-quality Zn-BDT thin films of the anticipated composition of  $(\text{Zn}-\text{S}-\text{C}_6\text{H}_6-\text{S})_n$ . The traces of nitrogen impurity observed presumably result from the Zn precursor used.

XPS (X-ray photoelectron spectroscopy) measurements were performed to investigate the film composition in detail (Figure 4; survey scans in Figure S5, Supporting Information). From Figure 4a, the characteristic split peaks of  $2p_{3/2}$  and  $2p_{1/2}$  are seen for zinc at 1022 and 1045 eV, respectively; these binding energy values are higher than those reported for  $\text{ZnS}$ <sup>[55]</sup> and metallic  $\text{Zn}(0)$ ,<sup>[56]</sup> but they nearly match the values reported

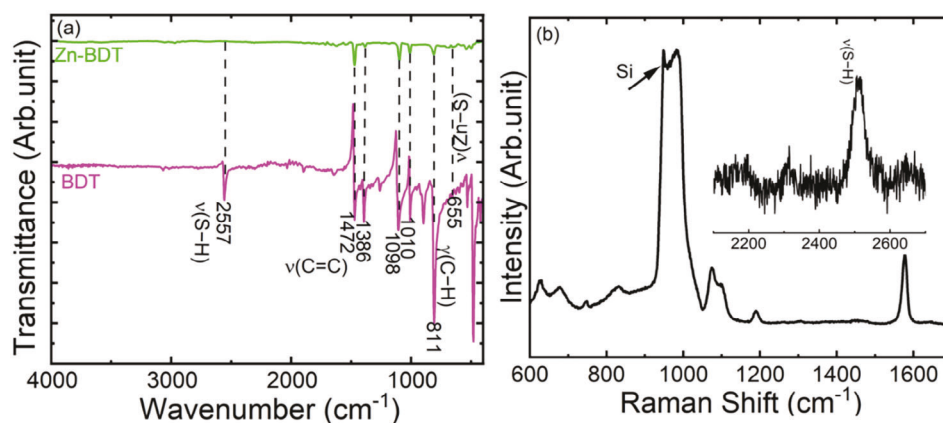


**Figure 2.** a) FTIR, and b) Raman spectra for a 90-nm thick Zn-BDT film. In (a), FTIR spectrum for BDT precursor is given for comparison. In (b), peak arising from Si substrate is indicated,<sup>[54]</sup> and  $\nu(\text{S-H})$  stretching vibration area from unreacted BDT is enlarged in insert.

for ZnS/graphene oxide composite.<sup>[57]</sup> The +II oxidation state for Zn is also evident from the  $\text{Zn}_{\text{LMM}}$  spectrum (Figure 4a, inset).<sup>[58]</sup> The S 2p spectrum (Figure 4b) indicates multiple species with varying coordination environments: thiolate (Zn-S-C) at 162.7 eV,<sup>[58]</sup> free thiol at 163.9 eV,<sup>[59]</sup> and sulfite/sulfate<sup>[60]</sup> at 167.4/168.9 eV.<sup>[50]</sup> The thiolate component (with an excellent match to reported thiolates)<sup>[58]</sup> has the strongest intensity as expected since it is the main bonding species in the film, while the sulfite and sulfate components most probably originate from some film surface species only, presumably resulting from the surface oxidation by air.

We confirmed this by performing the XPS analysis at different sputtering durations to study the film composition across its

depth (Figure S6 and Table S1, Supporting Information): as expected, the sulfite and sulfate components disappeared after the first sputtering step (Figure S6a and S6c, Supporting Information). Regarding the Zn/S ratio, the value (0.42) obtained from the non-sputtered XPS measurement is relatively close to the RBS result (0.5). With the increasing sputtering time the Zn/S ratio was found to increase most likely due to preferential sputtering of the lighter S over Zn.<sup>[61]</sup> Importantly, no change in the Zn 2p peak positions or relative intensities was observed (Figure S6b, Supporting Information). The amount of the free thiol was found higher at the surface (Table S1, Supporting Information) compared to the bulk of the film after the first sputtering steps. However, the free thiol did not disappear completely but remained

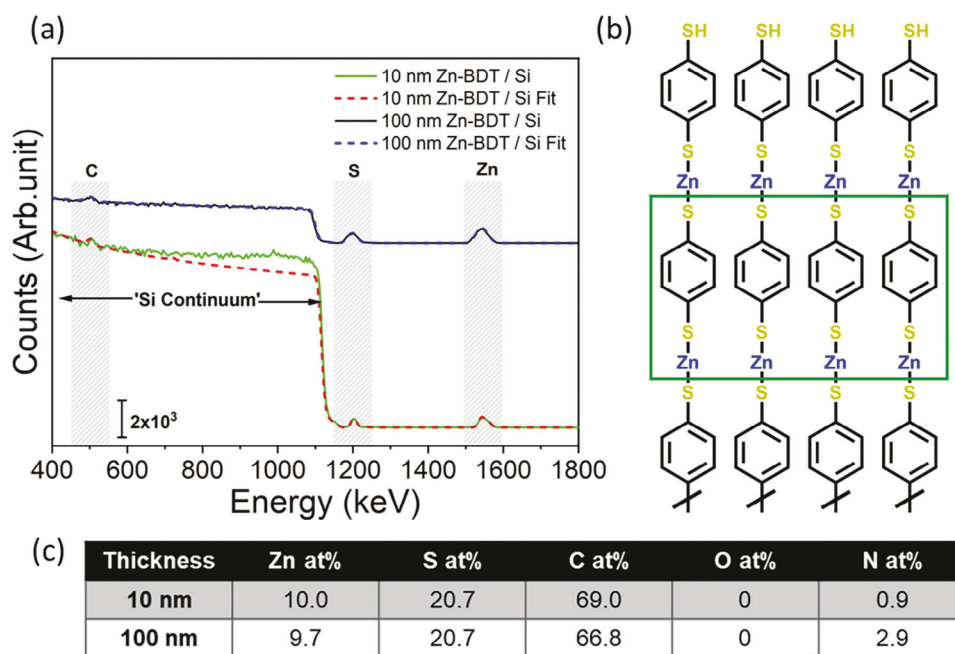


**Figure 3.** a) RBS spectra for two Zn-BDT films with different thicknesses. b) Schematic bonding structure of Zn-BDT where each Zn atom is bonded to two S atoms and therefore the Zn/S ratio is expected to be 0.5. This is highlighted with the green square which indicates the repeating layers and hence the expected Zn/S ratio in the films. c) Observed elemental composition distribution discerned from RBS.

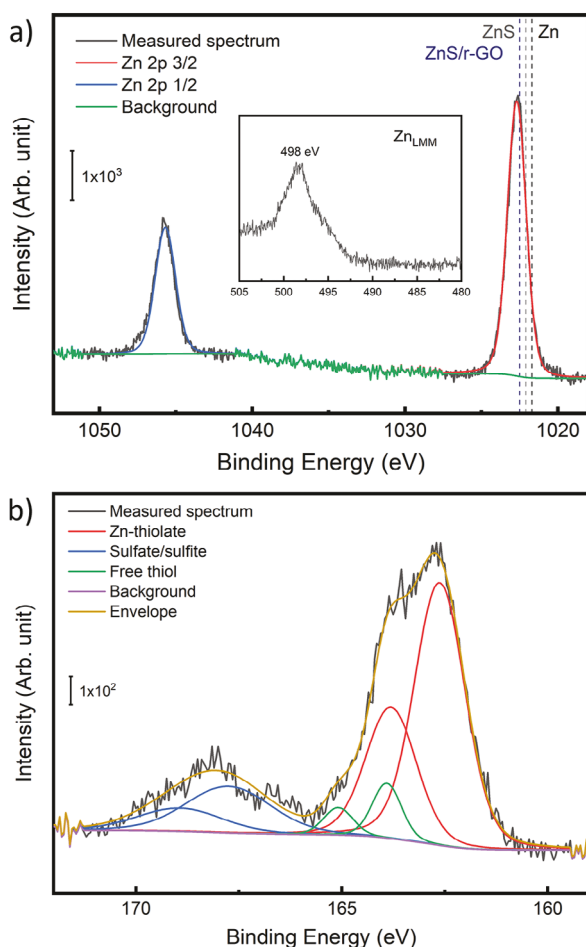


**Figure 4.** XPS spectra for a) Zn 2p, and b) S 2p components of a Zn-BDT film.

stable with further sputtering. This suggests that a small part of the thiol groups are left unreacted which can be caused by insufficient thermal energy at low temperatures<sup>[47]</sup> (60 °C) and steric hindrance caused by the relatively bulky BDT backbone.

A major drawback of the conventional organic-diol-based metalcone films regarding their potential applications (e.g., as barrier coatings) is their instability under ambient conditions. Almost all ALD/MLD-grown alucones and zincones reported so far have been found to undergo degradation within a few hours of storage in ambient conditions.<sup>[29,30,62]</sup> This degradation is typically seen as a clear drop in the film thickness, and an appearance of additional peaks in the FTIR spectrum due to water/OH groups. For our Zn-BDT thin films, both the FTIR pattern and the film thickness remained nearly unchanged even after 25 days of storage (increased by 1.7 nm) in ambient conditions, indicative of their superior air-stability (Figure 5).

We also addressed the long-term stability of the same Zn-BDT film with Raman mapping and FTIR analysis after one-year open-air storage of the film (Figure S7, Supporting Information). No drastic changes in Raman peak intensities were observed over the scanned area of 250  $\mu\text{m} \times 180 \mu\text{m}$ , indicating the excellent homogeneity of the film even after the one-year storage. In the

FTIR spectrum, an additional peak appeared at 1585  $\text{cm}^{-1}$  that can be assigned to the deformation vibration of  $\text{H}_2\text{O}$ ,  $\delta(\text{H}_2\text{O})$ ,<sup>[31]</sup> indicating some moisture absorption. However, the main peak intensities have remained essentially unchanged. Similar conclusion could be made from the XRR measurement for the film thickness: during the one-year storage the film thickness had increased only by 5.6 nm, that is, at an even slower rate than during the first 25 days. The observed increase in thickness is likely caused by the water absorption which might lead to a swelling but does not degrade the chemical composition of the Zn-BDT film based on the unchanged Raman/FTIR Zn-BDT signals of the aged film.

Contact angle measurements (Figure S8, Supporting Information) performed for both 10- and 100-nm films indicated hydrophobic behavior of the present Zn-BDT films, in line with the observed weak interaction with air/moisture. The contact angle (55.5°) observed for the 100-nm film is very close to the previously reported value for the stable thiol-based alucone films (59.4° for a 86.2-nm thick film).<sup>[44]</sup>

Another important characteristic regarding the potential future barrier coating applications is the high electrical resistance of the films. We confirmed this for the Zn-BDT thin films by measuring the electrical transport properties using both two-probe and four-probe resistance measurements. Irrespective of the thickness, the films were found to be highly insulating, and the resistivity was beyond the detection limit (10 M $\Omega$ ) of the instrument used. This is considered beneficial especially in applications where they are used as an encapsulation layer in printed circuit boards for protecting from external electrical influences.

Finally, we evaluated our  $[\text{Zn}(\text{DMP})_2] + \text{BDT}$  process regarding the conformality of the resultant Zn-BDT films using LHAR test chips; the advantage of these test structures is their easy characterization after the deposition which does not require any cross-sectional analyses (needed when using vertical high-aspect-ratio structures).<sup>[35,63]</sup> Here, with the LHAR chips used (Figure S9, Supporting Information) the top roof silicon membrane was simply removed after the Zn-BDT film deposition using an adhesive tape, thereby exposing the film for further analysis. The film penetration depth (PD) was evaluated by various ways. The most straightforward way was to use optical microscopy (Figure S10, Supporting Information). Most readily, an estimate for the PD value was obtained from an optical microscope image by visually observing the contrast difference between the deposited film and the uncoated cavity surface (Figure S10a,d, Supporting Information). For more comprehensive information, a thickness profile (film thickness as function of PD) of the image was obtained through optical microscope image analysis (Figure S10b,e, Supporting Information). From this profile curve we can readily define fractional PD values, for example, PD<sub>50%</sub> value is the film penetration depth up to which the film thickness is 50% or higher of the original film thickness at the cavity entrance (Figure S10c,f, Supporting Information). However, due to the relatively low visualization capability of optical microscopy (limited to ca. 15 nm films), it is not possible to follow the film growth up to the film-growth ending area where the zero-film growth limit is reached. Usually, the optical microscope approach facilitates the identification of PD<sub>50%</sub> value when the initially targeted film thickness is ca. 20 nm or higher, naturally also depending on the optical properties of the film material.<sup>[64]</sup> For the estimation of the total

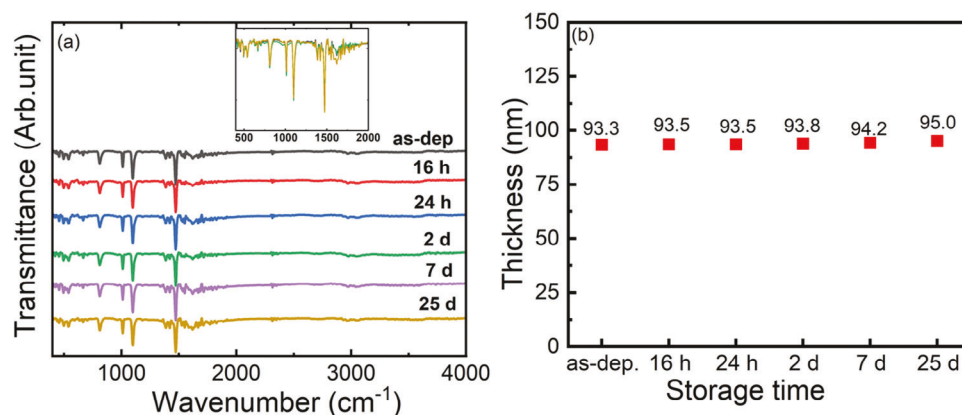


**Figure 5.** Stability studies for a representative Zn-BDT thin film: a) FTIR spectra (overlaid magnifications of the most intense features in the inset from samples as deposited and aged for 2 and 25 days), and b) XRR-determined film thickness values, measured for the film after indicated time periods during its storage in ambient conditions. The precise thickness value (nm) is given on top of each datum point to illustrate that during the air-storage the film thickness gradually but extremely slowly increases (by 1.7 nm in 25 days).

penetration depth ( $PD_{tot}$ ) values, SEM imaging was employed, as it enables higher resolution visualization of ultrathin layers deep inside the cavities (Figure S11a, Supporting Information). For the further confirmation of film thickness in the entire film coverage range, we utilized a line-scan reflectometry method (Figure S11b, Supporting Information).

The Zn-BDT film PD was found to depend on the precursor pulse lengths (Table 1; Figure S11b, Supporting Information). We started the LHAR experiments using the same deposition parameters as used with flat Si substrates; this resulted in relatively low PD values. Increasing the pulse lengths of both precursors increased the PD considerably. The  $PD_{tot}$  value doubled from 125 to 260  $\mu\text{m}$  when the pulse length was doubled from 30 to 60 s. Though an increase in pulse length increased the total PD, the thickness profile was similar regardless of the pulse length since the film thickness gradually decreased along the PD for both the 30-s and the 60-s pulse cases (Figure 6; Figure S11, Supporting Information). This indicates that the film uniformity is independent of the precursor pulse length though pulse length plays a major role in controlling the penetration of the film inside the cavity. Since the maximal film thickness was considerably low for the 60 s pulse sample (10 nm) and beyond the detecting limit of optical microscope, no contrast difference was observed in optical microscope images. However, both the SEM imaging and the line-scan reflectometry data indicated a deep growth inside the LHAR cavities (Figure 6). A change in contrast in the SEM im-

age due to the thickness reduction was observed at a penetration depth of 200  $\mu\text{m}$ . Similarly, a change in the shape of the thickness profile curve was discerned, indicating a sharp decrease in thickness was observed in the line-scan reflectometry analysis. The tailing observed in the thickness profile from line-scan measurements is primarily attributed to the increased noise level. The film coverage was same for both non-mirrored trenches (opening only to one side) and mirrored trenches (opening to both sides, Figure S12, Supporting Information), indicating a non-directional Zn-BDT film growth.

Concluding from the LHAR conformality tests, the Zn-BDT films are grown in an appreciably conformal manner with the target thickness at the start of the cavity followed by a relatively stable region in terms of film thickness before the rather abrupt thickness decrease. These are truly promising results and comparative to those demonstrated for alucone films grown from dimethylaluminum isopropoxide (DMAI) and ethylene glycol (EG) with atmospheric spatial ALD/MLD at 150  $^{\circ}\text{C}$ .<sup>[32]</sup> The DMAI + EG process yielded impressive conformality with essentially stable film thickness up to 200  $\mu\text{m}$  or even higher. On the other hand, the LHAR conformality reported for alucone films grown from trimethyl aluminium (TMA) and EG suffer from the infiltration of the small TMA precursor molecules which act as a kind of precursor reservoir in the films. This causes a significant CVD component and excessive film growth near the trench opening once the infiltrated (and thus slowly evacuated) gaseous TMA

**Table 1.** Penetration depth results based on optical microscopy ( $PD_{50\%}$ ) and on SEM ( $PD_{tot}$ ) data for three samples (Zn-BDT films on LHAR substrates) deposited with different ALD/MLD parameters (pulse/purge lengths and cycle numbers).

Pulsing sequence: $[\text{Zn}(\text{DMP})_2]/\text{purge}/\text{BDT}/\text{purge}$	ALD/MLD cycles/Film thickness [nm] <sup>a)</sup>	Penetration depth [ $\mu\text{m}$ ]	
		Opt: $PD_{50\%}$	SEM: $PD_{tot}$
3 s/20 s/3 s/20 s	115/50	26	–
30 s/30 s/30 s/30 s	115/56	67	125
60 s/60 s/60 s/60 s	20/11	–	260

<sup>a)</sup> measured for a film simultaneously deposited on a planar Si substrate.

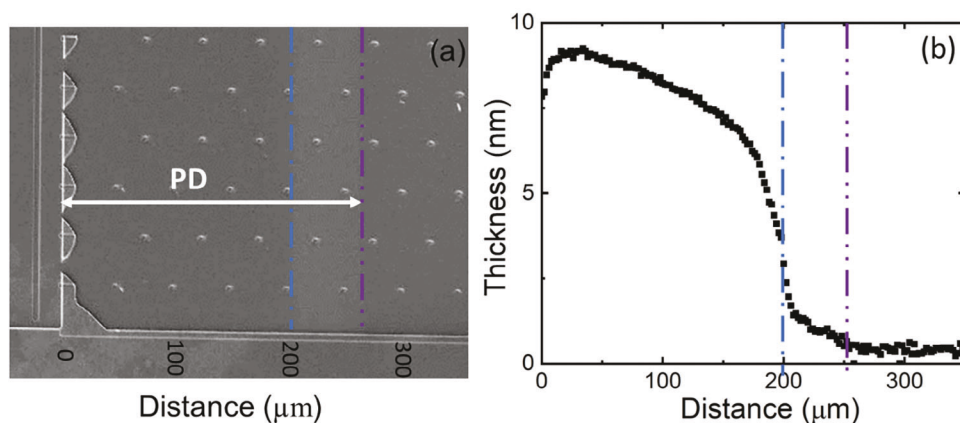


**Figure 6.** a) SEM image (distance between dots is 50  $\mu\text{m}$ ), and b) thickness profile from a film analyzer reflectometer, for a 10-nm Zn-BDT film grown into a non-mirrored cavity of LCHAR chip with a pulsing sequence: 60 s  $[\text{Zn}(\text{DMP})_2]/60$  s  $\text{N}_2/60$  s BDT/60 s  $\text{N}_2$ . The distances obtained from the SEM image for the thickness variation  $\approx 200$   $\mu\text{m}$  and the  $\text{PD}_{\text{tot}}$  value at 260  $\mu\text{m}$ , are marked with the broken lines on the thickness profile.

precursors react with the upcoming EG precursor pulse.<sup>[32]</sup> In the case of the bulkier  $[\text{Zn}(\text{DMP})_2]$  and DMAI precursors, similar infiltration phenomenon is less likely. The observed positive impact of precursor bulkiness on the conformality was similar to the recently reported results for LiPON thin films, showing that the bulkier Li-HMDS (lithium bis(trimethylsilyl)amide) precursor enhanced the conformality as compared to the smaller  $\text{LiO}^t\text{Bu}$  (lithium *tert*-butoxide).<sup>[33]</sup>

Finally, we investigated the chemical state of the Zn-BDT films deposited into the LCHAR structures. First, we collected Raman spectra from four different positions including the top-roof membrane (unpeeled) and at a length of 5, 35, and 60  $\mu\text{m}$  away from the membrane edge of the structure for a representative Zn-BDT film grown on the LCHAR substrate. First of all, in all the four spectra the peak features were found to be identical to the planar film. As for the intensities of these features, the intensities were essentially identical for the spectra measured for the film grown on the polysilicon roof (like planar substrate), and at a 5- $\mu\text{m}$  distance away from the membrane edge, indicating identical film thicknesses (Figure 7). After that the Raman signal intensity decreases as a function of distance from the membrane edge, in a manner following the film thickness profile. Similar to the planar film case, a weak signal at 2527  $\text{cm}^{-1}$  corresponding to unreacted BDT<sup>[53]</sup> was also observed for the LCHAR grown film. The observed data indicated a reduction in BDT signal intensity as a function of penetration depth, as anticipated from the decreasing film thickness.

Furthermore, XPS data were collected from three different positions: membrane edge,  $\text{PD}_{50\%}$ , and finally close to the film ending (Figure S13, Supporting Information). Both the Zn and S 2p peak positions (Figure 8) were equivalent to the measured planar film, thus indicating identical chemical state of the main chemical species in the LCHAR cavities. The signal intensities decrease with increasing film penetration as expected due to the decreasing film thickness. Also the Zn/S ratio decreases, from 0.72 at the membrane edge to 0.52 at  $\text{PD}_{50\%}$  and 0.35 at the film ending (Table S2, Supporting Information), possibly due to a higher sticking coefficient of  $[\text{Zn}(\text{DMP})_2]$  in comparison to BDT, resulting in Zn-rich cavity entry. Additionally, the XPS analysis indicated an increased oxygen content (Figure 8b; Table S2, Support-

ing Information) due to an increased sulfite/sulfate concentration deep in the cavity, thus indicating increased oxidation of S deeper in the trenches. This is reasonable due to the increased S content with respect to Zn and hence increased content of unreacted thiol which can be prone to oxidation.

### 3. Conclusion

A novel low-temperature ALD/MLD process for the fabrication of high-quality amorphous thin films of a new Zn-based hybrid material, Zn-BDT was developed. This process is based on the

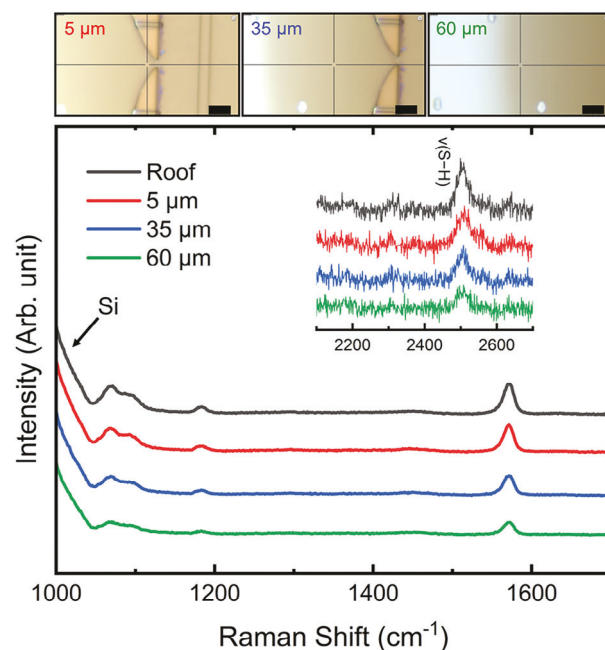


**Figure 7.** Raman spectra collected from a Zn-BDT film deposited into a LCHAR test structure as a function of distance from the membrane edge; the areas from which the data are collected are given in the top row. Weak signal corresponding to unreacted BDT observed at  $\approx 2500$   $\text{cm}^{-1}$  is given in the insert. Scale bar in the top row images is 10  $\mu\text{m}$ .

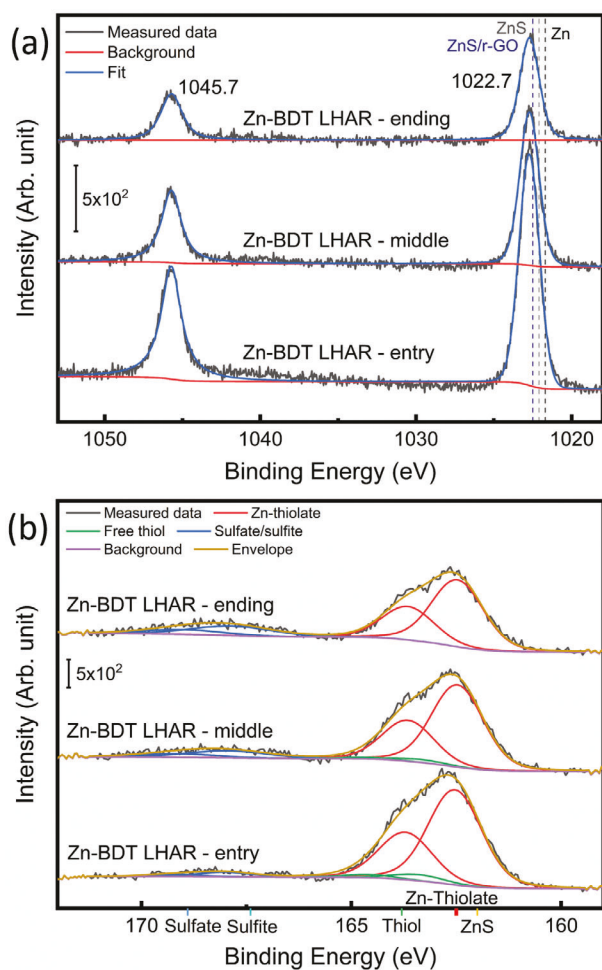


**Figure 8.** XPS spectra of a) Zn 2p, and b) S 2p components for a Zn-BDT film deposited on a LHAR structure, recorded from the beginning, middle, and end of the cavity.

reactive and non-pyrophoric zinc precursor  $[\text{Zn}(\text{DMP})_2]$  and the less explored benzene-1,4,-dithiol as the organic precursor. The relatively high vapor pressures, safe handling (non-pyrophoricity of  $[\text{Zn}(\text{DMP})_2]$ ), and excellent reactivity even at low temperatures were the major criteria for selecting these precursors for the aimed low deposition temperature process.

The newly developed ALD/MLD process yielded highly homogeneous thin films with an appreciably high growth rate of  $4.5 \text{ \AA}/\text{cycle}$  at  $60 \text{ }^\circ\text{C}$ . The possible low-temperature condensation and high-temperature decomposition of the precursors could be ruled out. The targeted chemical composition of  $(\text{Zn}-\text{S}-\text{C}_6\text{H}_6-\text{S})_n$  was confirmed using different analytical techniques including XPS, RBS, FTIR, and Raman analysis.

The Zn-BDT films were found to be electrically insulating and appreciably stable under ambient conditions over extended storage periods, which are highly encouraging properties considering their potential application area, that is, barrier coatings in microelectronics. Also importantly, using state-of-the-art LHAR test structures we could demonstrate that by increasing the precursor pulse lengths it was possible to extend the essentially ideal film growth deep into the high-aspect-ratio cavities. The promis-

ing conformality characteristics and excellent air-stability thus demonstrated for the Zn-BDT films are beneficial factors for employing these films in highly demanding insulating barrier layers in temperature sensitive microelectronics.

#### 4. Experimental Section

The Zn-BDT films were grown using in-house synthesized  $[\text{Zn}(\text{DMP})_2]$  (bis-3-(*N,N*-dimethylamino)propyl zinc)<sup>[14]</sup> and commercial BDT (benzene-1,4,-dithiol; Sigma-Aldrich) precursors, placed in open boats inside the reactor (flow-type hot-wall ALD reactor; F-120 by ASM Microchemistry Ltd, Figure S1, Supporting Information) where they were both heated to  $35 \text{ }^\circ\text{C}$  for evaporation (based on our previous experience using these precursors in other processes).<sup>[31,43]</sup> Nitrogen (>99.999%, Schmidlin UHPN 3000  $\text{N}_2$  generator) was used as a carrier and purging gas, and the pressure inside the reactor was maintained between 3–4 mbar. The precursor pulse lengths and the deposition (substrate heating) temperature were optimized in the study.

For the process development and optimization, the depositions were carried out on  $2.0 \times 2.0 \text{ cm}^2$  Si(100) substrates (Okmetic Oy). The success of the film growth was routinely evaluated using X-ray reflectivity measurements (XRR; X'Pert MPD PROAlfa 1, PANalytical,  $\text{Cu K}\alpha$ ). The XRR patterns were fitted with X'Pert Reflectivity software by PANalytical for the film thickness, density, and roughness. The growth-per-cycle (GPC) value was calculated by dividing the film thickness by the number of deposition cycles applied. The density ( $\rho_e$ ) values were calculated from the critical angle ( $\theta_c$ ) as  $\rho_e = (2\pi \theta_c) / (\lambda 2r_e)$ , where  $\lambda$  is the X-ray wavelength used and  $r_e$  is the classical electron radius.

AFM measurements of selected samples were conducted using a JPK NanoWizard 3 device in the tapping mode at a frequency of 218 kHz, a line rate of 1 Hz, and a scan resolution of  $512 \times 512$  pixels. Recorded images were further analyzed using Gwyddion software<sup>[65]</sup> to access the root-mean-square (RMS) roughness of the analyzed samples. The water contact angle was measured on an SEO Phoenix 150 device using deionized water at room temperature. The contact angles were evaluated using the corresponding SEO Image XP software suite.

For confirming the completion of the surface reactions and investigating the types of chemical bonding involved in the Zn-BDT thin films both Fourier transform infrared (FTIR; Bruker alpha II) and Raman measurements (Witec Raman with a 532 nm excitation wavelength) were carried out. The FTIR measurements were performed in a transmission mode in the range of  $400\text{--}4000 \text{ cm}^{-1}$ . The resolution was  $4 \text{ cm}^{-1}$  and each given spectrum was an average of 24 measured spectra. For removing the interference from silicon, blank Si spectrum was subtracted from the thin film spectra. Tescan Mira3 scanning electron microscope (SEM) using an acceleration voltage of 10 kV was used for measuring the penetration depth (PD) of the film inside the LHAR cavity.

For the determination of the Zn/S atomic ratio in the Zn-BDT films, Rutherford backscattering spectrometry (RBS) was utilized. The RBS experiments were performed at the RUBION facility (Ruhr University Bochum); the beam ( $2.0 \text{ MeV } 4\text{He}^+$  ions, intensity 20–40 nA) penetrated the whole film at an angle of  $7^\circ$ . Scattered particles were observed by a solid-state detector which was placed at an angle of  $160^\circ$ . To systematically analyze the obtained RBS spectra, software SIMNRA was used. Additionally, to obtain further information for the chemical composition/state, X-ray photoelectron spectroscopy (XPS) measurements were performed (PHI5000 instrument; the source was operated at 10 kV and 24.6 W using  $\text{Al K}\alpha$  (1486.6 eV) radiation at a  $45^\circ$  electron take-off angle. The kinetic energy of the electrons was analyzed by a spherical Leybold EA-10/100 analyzer using a pass energy of 18 eV. A selected Zn-BDT thin film sample was analyzed by a combination of survey scans and core level scans for peaks of interest. Step widths of 0.5 and 0.05 eV were adjusted for the survey and core level scans, respectively. The pressure of the analysis chamber was maintained at  $<10^{-7}$  mbar. For a planar thin film, scans were done on the as introduced surface followed by scans after a succession of Ar+ sputter steps. Mild sputtering condition ( $1 \times 0.5 \text{ min}$ , 500 V,  $2 \times 2$ ) were

employed to avoid damaging the organic components. For a LHAR sample, measurements were performed only on the as introduced surface but with three different locations along the substrate cavities. The position of the final measurement locations were estimated by using a camera integrated into the device and finding the exact location by checking the signal intensities for various spots along the cavities, hence finding the precise location for the start of the cavity and end of the film. Deconvolution analysis of the core level signals was completed by Shirley background processing and Gaussian functions using UniFit 2017 software.<sup>[66,67]</sup>

For the conformality studies, the depositions were performed on PillarHall LHAR (LHAR4) test structures (Chipmetrics Ltd).<sup>[35,63,68]</sup> A reference silicon wafer was also placed with a LHAR substrate in every deposition and the film thickness on the reference substrate was determined using XRR. The important benefit in using these LHAR chips is that there is no need for cross sectioning, which is unavoidable with the conventional vertical holes approach.<sup>[69,70]</sup> After the film deposition into the PillarHall LHAR chips, the top-roof polysilicon membrane from the LHAR structure was simply removed using adhesion tape method. For this, a small piece of adhesion tape was gently glued on the upper half of the thin film and then pulled away to peel off the polysilicon membrane from that side and thereby exposing the film to analysis, see Figure S9 (Supporting Information) for the schematics of the LHAR substrate structure. Then, it is in principle possible to use any analytical technique that is compatible to planar materials, to assess the film growth conformality. Another advantage in using PillarHall LHAR structures for conformality studies is that the conformality data produced with LHAR structures can be used to predict conformality for any other target structures with known dimensions and shapes under similar reaction conditions using the modeling method by Gordon et al.<sup>[69]</sup> For LHAR structures, the aspect ratio ( $\alpha$ ) is  $L/2g$  and for a vertical high aspect ratio (VHAR) it is  $L/g$ , where  $L$  and  $g$  are the penetration depth and gap height, respectively. With the knowledge of penetration depth and gap height for LHAR structures and the gap height (hole diameter) of VHAR structures, it is thus possible to calculate the predicted penetration depth or conformality for the VHAR structures.

In the present study, optical microscopy (Euromex Holland) was used for imaging the film grown on the LHAR substrate, and penetration depth calculations were done from the optical microscope images. Thin film analyzer reflectometer with scanning XY-stage (Filmetrics F40-UVX) was used for thickness profile measurement. The movement of sample stage in x-y direction enables performing thickness map of the samples. The model used for reflectometry measurement comprised of a bottom Si substrate with few nm native oxide and a top layer of the grown Zn-BDT thin film. The measurement is indirect, being based on modeling the reflectance spectrum that best fits the measured film thickness. The complex refractive index  $n$  and the extinction coefficient  $k$  were not readily available and were determined using prior knowledge of the film thickness in the opening area of the LHAR structure. Empirically, the Bruggeman model was found to give a good estimation for  $n$  and  $k$ . The determined refractive index was used to fit the film thickness for each measured locations along the penetration depth profile.

## Supporting Information

Supporting Information is available from the Wiley Online Library or from the author.

## Acknowledgements

A.P. and T.J. contributed equally to this work. Funding was received from the European Union (ERC AdG, UniEnMLD, No. 101097815). Views and opinions expressed are however those of the authors only and do not necessarily reflect those of the European Union or the European Research Council. Neither the European Union nor the granting authority can be held responsible for them. The authors from RUB and IFW thank the DFG REACTIVE project (number 490773082) and the Leibniz Association for supporting this work.

## Conflict of Interest

The authors declare no conflict of interest.

## Data Availability Statement

The data that support the findings of this study are available from the corresponding author upon reasonable request.

## Keywords

air-stability, atomic/molecular layer deposition, conformality, low-temperature deposition, metal-organic thin film

Received: April 2, 2024  
Revised: May 17, 2024  
Published online: June 9, 2024

- [1] X. Meng, *J. Mater. Chem. A* **2017**, *5*, 18326.
- [2] J. Multia, M. Karppinen, *Adv. Mater. Interfaces* **2022**, *9*, 2200210.
- [3] H. Zhou, S. F. Bent, *J. Vac. Sci. Technol. A* **2013**, *31*, 040801.
- [4] P. Sundberg, M. Karppinen, *Beilstein J. Nanotechnol.* **2014**, *5*, 1104.
- [5] T. Suntola, *Mater. Sci. Rep.* **1989**, *4*, 261.
- [6] S. M. George, *Chem. Rev.* **2010**, *110*, 111.
- [7] A. Khayyami, A. Philip, M. Karppinen, *Angew. Chem., Int. Ed.* **2019**, *58*, 13400.
- [8] M. Nisula, J. Linnera, A. J. Karttunen, M. Karppinen, *Chem. – Eur. J.* **2017**, *23*, 2988.
- [9] J. Han, T. Kim, D. Kim, H. L. Yang, J. Park, *Dalton Trans.* **2021**, *50*, 15841.
- [10] Y. Li, Y. Xiong, H. Yang, K. Cao, R. Chen, *J. Mater. Res.* **2020**, *35*, 681.
- [11] M. Park, S. Oh, H. Kim, D. Jung, D. Choi, J. S. Park, *Thin Solid Films* **2013**, *546*, 153.
- [12] O. Lidor-shalev, N. Leifer, M. Eigenberg, H. Aviv, I. Perelshtein, G. Goobes, M. Noked, Rosy, *Batteries Supercaps* **2021**, *4*, 1739.
- [13] D. M. Piper, Y. Lee, S. B. Son, T. Evans, F. Lin, D. Nordlund, X. Xiao, S. M. George, S. H. Lee, C. Ban, *Nano Energy* **2016**, *22*, 202.
- [14] L. Mai, F. Mitschker, C. Bock, A. Niesen, E. Ciftiyurek, D. Rogalla, J. Mickler, M. Erig, Z. Li, P. Awakowicz, K. Schierbaum, A. Devi, *Small* **2020**, *16*, 1907506.
- [15] J.-P. Niemelä, A. Philip, N. Rohbeck, M. Karppinen, J. Michler, I. Utke, *ACS Appl. Nano Mater.* **2021**, *4*, 1692.
- [16] A. Philip, J. P. Niemelä, G. C. Tewari, B. Putz, T. E. J. Edwards, M. Itoh, I. Utke, M. Karppinen, *ACS Appl. Mater. Interfaces* **2020**, *12*, 21912.
- [17] Z. Giedraityte, P. Sundberg, M. Karppinen, *J. Mater. Chem. C* **2015**, *3*, 12316.
- [18] B. Yoon, B. H. Lee, S. M. George, *J. Phys. Chem. C* **2012**, *116*, 24784.
- [19] A. I. Abdulgatov, R. A. Hall, J. L. Sutherland, B. H. Lee, A. S. Cavanagh, S. M. George, *Chem. Mater.* **2012**, *24*, 2854.
- [20] D. W. Choi, M. Yoo, H. M. Lee, J. Park, H. Y. Kim, J. S. Park, *ACS Appl. Mater. Interfaces* **2016**, *8*, 12263.
- [21] B. H. Lee, B. Yoon, A. I. Abdulgatov, R. A. Hall, S. M. George, *Adv. Funct. Mater.* **2013**, *23*, 532.
- [22] A. A. Dameron, D. Seghete, B. B. Burton, S. D. Davidson, A. S. Cavanagh, J. A. Bertrand, S. M. George, *Chem. Mater.* **2008**, *20*, 3315.
- [23] Q. Peng, B. Gong, R. M. VanGundy, G. N. Parsons, *Chem. Mater.* **2009**, *21*, 820.
- [24] B. H. Lee, V. R. Anderson, S. M. George, *ECS Trans.* **2011**, *41*, 131.
- [25] Z. Chen, H. Wang, X. Wang, P. Chen, Y. Liu, H. Zhao, Y. Zhao, Y. Duan, *Sci. Rep.* **2017**, *7*, 40061.
- [26] S. Feng-Bo, D. Yu, Y. Yong-Qiang, C. Ping, D. Ya-Hui, W. Xiao, Y. Dan, X. Kai-Wen, *Org. Electron.* **2014**, *15*, 2546.

- [27] M. Vähä-Nissi, P. Sundberg, E. Kauppi, T. Hirvikorpi, J. Sievänen, A. Sood, M. Karppinen, A. Harlin, *Thin Solid Films* **2012**, 520, 6780.
- [28] D. Choudhury, G. Rajaraman, S. K. Sarkar, *RSC Adv.* **2015**, 5, 29947.
- [29] D. Choudhury, S. K. Sarkar, N. Mahuli, *J. Vac. Sci. Technol. A* **2015**, 33, 01A115.
- [30] M. Aghaee, J. P. Niemelä, W. M. M. Kessels, M. Creatore, *Dalton Trans.* **2019**, 48, 3496.
- [31] A. Philip, L. Mai, R. Ghiyasi, A. Devi, M. Karppinen, *Dalton Trans.* **2022**, 51, 14508.
- [32] H. Jain, M. Creatore, P. Poodt, *J. Vac. Sci. Technol. A* **2023**, 41, 012401.
- [33] M. Madadi, M. Heikkinen, A. Philip, M. Karppinen, *ACS Appl. Electron. Mater.* **2024**, 6, 1574.
- [34] K. Arts, S. Deijkers, R. L. Puurunen, W. M. M. Kessels, H. C. M. Knoop, *J. Phys. Chem. C* **2021**, 125, 8244.
- [35] V. Cremers, R. L. Puurunen, J. Dendooven, *Appl. Phys. Rev.* **2019**, 6, 021302.
- [36] K. Arts, M. Utriainen, R. L. Puurunen, W. M. M. Kessels, H. C. M. Knoop, *J. Phys. Chem. C* **2019**, 123, 27030.
- [37] J. Huang, A. T. Lucero, L. Cheng, H. J. Hwang, M. W. Ha, J. Kim, *Appl. Phys. Lett.* **2015**, 106, 123101.
- [38] F. Krahl, A. Giri, J. A. Tomko, T. Tynell, P. E. Hopkins, M. Karppinen, *Adv. Mater. Interfaces* **2018**, 5, 1701692.
- [39] R. Ghiyasi, G. C. Tewari, M. Karppinen, *J. Phys. Chem. C* **2020**, 124, 13765.
- [40] K. B. Lausund, M. S. Olsen, P. A. Hansen, H. Valen, O. Nilsen, *J. Mater. Chem. A* **2020**, 8, 2539.
- [41] M. Rogowska, P. A. Hansen, H. H. Sønsteby, J. Dziadkowiec, H. Valen, O. Nilsen, *Dalton Trans.* **2021**, 50, 12896.
- [42] K. B. Klepper, O. Nilsen, H. Fjellvåg, *Dalton Trans.* **2010**, 39, 11628.
- [43] D. J. Hagen, L. Mai, A. Devi, J. Sainio, M. Karppinen, *Dalton Trans.* **2018**, 47, 15791.
- [44] G. Baek, S. Lee, J.-H. Lee, J.-S. Park, *J. Vac. Sci. Technol. A* **2020**, 38, 022411.
- [45] J. Multia, J. Heiska, A. Khayami, M. Karppinen, *ACS Appl. Mater. Interfaces* **2020**, 12, 41557.
- [46] N. M. Adamczyk, A. A. Dameron, S. M. George, *Langmuir* **2008**, 24, 2081.
- [47] P. Schweizer, L. M. Vogl, X. Maeder, I. Utke, J. Michler, *Adv. Mater. Interfaces* **2024**, 11, 2301064.
- [48] A. Sood, P. Sundberg, M. Karppinen, *Dalton Trans.* **2013**, 42, 3869.
- [49] E. Ahvenniemi, M. Karppinen, *Dalton Trans.* **2016**, 45, 10730.
- [50] A. Philip, S. Vasala, P. Glatzel, M. Karppinen, *Dalton Trans.* **2021**, 50, 16133.
- [51] J. Fahleisch, M. Fahland, W. Schönberger, N. Schiller, *Thin Solid Films* **2009**, 517, 3075.
- [52] J. P. Niemelä, M. Karppinen, *Dalton Trans.* **2015**, 44, 591.
- [53] S. H. Cho, H. S. Han, D.-J. Jang, K. Kim, M. S. Kim, *J. Phys. Chem.* **1995**, 99, 10594.
- [54] W. J. Lee, Y. H. Chang, *Coatings* **2018**, 8, 431.
- [55] D. Barreca, A. Gasparotto, C. Maragno, E. Tondello, T. R. Spalding, *Surf. Sci. Spectra* **2002**, 9, 54.
- [56] F. Cocco, B. Elsener, M. Fantauzzi, D. Atzei, A. Rossi, *RSC Adv.* **2016**, 6, 31277.
- [57] L. k. Mao, F. Wang, J. Mao, *Sci. Rep.* **2020**, 10, 62037.
- [58] P. Lang, C. Nogues, *Surf. Sci.* **2008**, 602, 2137.
- [59] D. G. Castner, K. Hinds, D. W. Grainger, *Langmuir* **1996**, 12, 5083.
- [60] G. Pan, J. Chen, K. Ge, L. Yang, F. Li, Z. Wang, S. Shi, X. Yang, Z. Zhou, A. Tang, W. Liu, Y. Sun, *J. Mater. Chem. C* **2019**, 7, 4449.
- [61] J. Sundberg, R. Lindblad, M. Gorgoi, H. Rensmo, U. Jansson, A. Lindblad, *Appl. Surf. Sci.* **2014**, 305, 203.
- [62] M. Ruoho, N. Tarasiuk, N. Rohbeck, C. Kapusta, J. Michler, I. Utke, *Mater. Today Chem.* **2018**, 10, 187.
- [63] F. Gao, S. Arpiainen, R. L. Puurunen, *J. Vac. Sci. Technol. A* **2015**, 33, 010601.
- [64] M. Utriainen, K. Saastamoinen, H. Rekola, O. M. E. Ylivaara, R. L. Puurunen, P. Hyttinen, *SPIE – Intl. Soc. Opt. Eng.* **2022**, 12008, 120080D.
- [65] D. Nečas, P. Klapetek, *Cent. Eur. J. Phys.* **2012**, 10, 181.
- [66] R. Hesse, T. Chassé, R. Szargan, *Anal. Bioanal. Chem.* **2003**, 375, 856.
- [67] R. Hesse, T. Chassé, R. Szargan, *Fresenius J. Anlyt. Chem.* **1999**, 365, 48.
- [68] M. L. van de Poll, H. Jain, J. N. Hilfiker, M. Utriainen, P. Poodt, W. M. M. Kessels, B. Macco, *Appl. Phys. Lett.* **2023**, 123, 182902.
- [69] R. G. Gordon, D. Hausmann, E. Kim, J. Shepard, *Chem. Vap. Depos.* **2003**, 9, 73.
- [70] J. S. Becker, S. Suh, S. Wang, R. G. Gordon, *Chem. Mater.* **2003**, 15, 2969.